atmosphere

MDPI

Article

Projected Increase in Clear-Air Turbulence over Southwest China Under Climate Change

Ruping Zhang, Zhigang Cheng, Wenjun Sang, Yu Huang * and Tingwei Cao

College of Aviation Meteorology, Civil Aviation Flight University of China, Guanghan 618307, China; zhangruping2001@163.com (R.Z.); chengzg@cafuc.edu.cn (Z.C.); sangwj@cafuc.edu.cn (W.S.); caotw@cafuc.edu.cn (T.C.)

* Correspondence: jadedr123@163.com

Abstract

Changes in aviation turbulence at cruise altitudes have important implications for aviation safety under global warming scenarios in the future. Using projections from the NorESM2-MM model within the CMIP6 framework, this study evaluates changes in clear-air turbulence (CAT) at 250 hPa over Southwest China during the twenty-first century based on an ensemble of 15 diagnostic indices. The results show: (1) Historical moderate-or-greater (MOG) CAT peaks in a zonal belt near 30–35° N, with annual frequencies up to 1.6% over the Hengduan and Karakoram Mountains. Future increases remain focused in this belt, are stronger and more extensive under SSP5-8.5, peak in winter and spring, and weaken over much of the Plateau interior in summer. (2) Future changes are intensity-dependent: stronger categories show larger relative increases, and PDF changes are concentrated in the right tail, indicating amplified extreme turbulence. The 19-year moving-average time series shows that MOG-CAT increases by 28.3% and 36.5% under SSP2-4.5 and SSP5-8.5, respectively, by the mid-twenty-first century, and by 26.0% and 69.4% by the late twenty-first century. (3) Along the Chengdu–Lhasa corridor, winter MOG-CAT increases in all three segments. Under SSP5-8.5, median increases are about 50% in the Basin and Plateau segments and about 85% in the Transition segment, with most diagnostics ranging from 50% to 180%. (4) High-emission scenarios are more likely to cause turbulence and instability in the southwestern region, potentially posing greater challenges for aviation turbulence warning and safety assurance.

Keywords: clear-air turbulence; CMIP6; Southwest China; aviation safety; climate change

Check for updates

Academic Editors: Jie Zhang, Wenli Lai and Pengtao Wang

Received: 15 March 2026
Revised: 5 April 2026
Accepted: 11 April 2026
Published: 15 April 2026

Copyright: © 2026 by the authors. Licensee MDPI, Basel, Switzerland. This article is an open access article distributed under the terms and conditions of the Creative Commons Attribution (CC BY) license.

1. Introduction

Clear-Air Turbulence (CAT) typically occurs in regions of strong wind shear near upper-level jet streams, characterized by the absence of visible clouds and separation from convective storm activity [1,2]. Owing to the lack of visual references and the limited detection capabilities of current satellite and airborne weather radars [3], CAT remains a primary meteorological hazard to modern aviation safety. Severe turbulence is widely recognized as a major contributor to in-flight injuries, operational disruptions, and flight delays or diversions, imposing significant economic losses on the global aviation industry.

Dynamically, CAT primarily originates from the Kelvin–Helmholtz (KH) instability, and its subsequent breaking is triggered within regions of strong atmospheric shear [4–6]. As the core environment for CAT generation, jet streams contain intense

vertical wind shear that significantly reduces the Richardson number (Ri), thereby facilitating the onset of atmospheric instability [7–10]. Furthermore, geostrophic adjustment processes near jet exit regions [2,11,12], mountain lee waves, and inertia-gravity waves excited by complex topography [13–15] are recognized as critical sources of CAT. The evolution of jet structures, such as confluence or curvature, modulates the intensity and spatial distribution of turbulence by enhancing the horizontal deformation field [16–18].

Extensive research indicates that climate change significantly alters the spatiotemporal distribution of CAT by modifying the large-scale circulation background. Driven by the thermal wind relation, the increased meridional temperature gradient in the upper troposphere, a result of global warming, strengthens mid-latitude jet streams and their associated vertical wind shear [7,19,20]. Climate model simulations generally project that by the mid-to-late 21st century, the frequency and intensity of moderate-or-greater (MOG) CAT along major global flight routes, such as the North Atlantic, North Pacific, and Europe, will increase substantially [6,21,22]. Notably, this increase exhibits a distinct tail-thickening characteristic, implying that the probability of extreme turbulence events is rising at a rate far exceeding that of the mean state [3,6]. Long-term trends in observational and reanalysis data corroborate this projection: the increasing frequency of CAT over the past four decades is highly consistent with the enhancement of jet shear under greenhouse gas forcing [23–25].

Although diagnosing CAT risks using Global Climate Models (GCMs) has been widely applied and validated in regions such as the North Atlantic [25,26], dedicated assessments for regions with complex terrain, where interactions between topography and upper-level jet streams are prominent, remain relatively scarce. Southwest China, situated at the convergence zone of the Tibetan Plateau and Sichuan Basin, is influenced by unique mechanical and thermal forcing associated with this complex topography. It serves as both a key maintenance area for the winter subtropical westerly jet and as a hotspot for high-altitude turbulence. As one of the most densely utilized airspaces in China's aviation network, covering core hubs such as Chengdu and Chongqing, this region handles a high volume of cross-regional and international flight traffic. However, existing studies have largely relied on earlier Coupled Model Intercomparison Project Phase 5 (CMIP5) models or single reanalysis datasets, whose spatiotemporal resolutions often constrain the accurate representation of circulation features under terrain jet interactions. Moreover, previous research has predominantly focused on mean trends, lacking a systematic quantification of extreme turbulence events based on the framework of the latest Coupled Model Intercomparison Project Phase 6 (CMIP6) [27].

To address these gaps, the present study utilized high-resolution atmospheric outputs from the NorESM2-MM model, which has demonstrated superior skill in representing upper-level winds and dynamic variables within the CMIP6 suite. Focusing on the 250 hPa cruising altitude, we construct an ensemble assessment framework incorporating 15 independent diagnostic indices to minimize physical uncertainties inherent in individual parameterizations.

We evaluate future projections under two SSP scenarios: SSP2-4.5 (a middle of the road, intermediate emission pathway) and SSP5-8.5 (a high emission, fossil fuel intensive scenario). The primary objectives of this study are: (1) to quantitatively project the spatiotemporal evolution and seasonal sensitivity of MOG-CAT frequency under these two future scenarios, using a fixed-threshold approach derived from the historical 99.6th percentile climatology (1985–2014); (2) to characterize the intensification of extreme turbulence probabilities through probability density functions (PDFs) tail analysis; and (3) to perform a corridor-based risk assessment for the critical Chengdu–Lhasa route using actual eAIP navigation data, segmented into topographic zones to discern the modulating role of the

mountain-basin transition. These findings provide a scientific framework for adaptive route planning and safety warnings in the increasingly complex and turbulent environment of Southwest China.

2. Materials and Methods

This study utilized daily atmospheric output from the second generation of the Norwegian Earth System Model (NorESM2-MM, v2; Norwegian Climate Centre, Oslo, Norway, abbreviated as NorESM2), a high-resolution model participating in Phase 6 of the Coupled Model Intercomparison Project (CMIP6) [28–30]. We archived comprehensive datasets spanning the historical baseline period (1985–2014) and the future projection period (2015–2094) for two Shared Socioeconomic Pathway (SSP) scenarios: SSP2-4.5 (moderate emissions) and SSP5-8.5 (high emissions). The NorESM2 model provides a horizontal resolution of $1.25^\circ \times 0.94^\circ$, and data were extracted between 200 and 250 hPa, which corresponds to the typical cruising altitudes of commercial aircraft.

To choose the appropriate model for our analysis within the CMIP6 suite, we carefully investigated the evaluation results provided by the Program for Climate Model Diagnosis and Intercomparison (PCMDI, https://pcmdi.llnl.gov/research/metrics/mean_clim, accessed on 4 April 2026) [31,32]. First, candidates were assessed based on their spatiotemporal root-mean-square errors (RMSE) against ERA5 reanalysis data. NorESM2 exhibited top-ranked skills in reproducing historical upper-level background fields, particularly for 200 hPa winds and temperature. Second, we examined the availability of specific meteorological variables required to calculate the turbulence diagnostics. Among the top-performing models, NorESM2 was uniquely capable of providing all the essential variables, including zonal wind (u), meridional wind (v), air temperature (t), and geopotential height (z), at a sufficient spatial resolution. Although daily mean data may smooth some extremes, they have been widely used for diagnosing long-term climatological changes in upper-level turbulence and have been shown to yield highly consistent spatial and probability distributions when compared with 6-hourly data [11,19,21]. Using these variables, this study calculated 15 CAT diagnostic indices (Table 1).

Table 1. Descriptions of the turbulence diagnostics used in this study.

Diagnostic	Description [33,34]
VWS	Vertical shear of horizontal wind
|DIV|	Magnitude of horizontal divergence
DEF^2	Total deformation squared
HTG	Magnitude of the horizontal temperature gradient
|V|	Horizontal wind speed
Brown	Composite of absolute vorticity, deformation, and vertical wind shear
Ellrod1	The product of vertical wind shear and deformation
Ellrod2	Vertical wind shear multiplied by the difference between deformation and horizontal divergence
Dutton	Dutton's empirical index
Endlich	Wind speed multiplied by turning
NGM1	Wind speed multiplied by deformation
NGM2	Magnitude of vertical temperature gradient multiplied by deformation
NVA	Negative vorticity advection
Ri^{-1}	Inverse Ri
$VORT^2$	Vertical vorticity squared

While climate models cannot explicitly resolve microscale clear-air turbulence (CAT), the 15 diagnostic indices listed in Table 1 are widely used to capture the large-scale atmospheric conditions conducive to CAT generation [34]. As established in atmospheric dynamics, these indices correlate with CAT through three well-established physical mech-

anisms. (1) Indices related to wind shear and kinematics (e.g., VWS, Speed, Vorticity, Divergence) quantify the shear-driven reduction in the Richardson number (Ri). When Ri falls below its critical threshold (typically Ri < 0.25), destabilizing inertial forces can overcome buoyant stability, triggering Kelvin-Helmholtz instability, which is widely considered the primary mechanism responsible for CAT [4–6]. Vorticity and divergence further help identify dynamically active regions, such as curved jet-stream segments and jet entrance/exit zones, where ageostrophic secondary circulations often amplify vertical shear. (2) Thermodynamic indices (e.g., HTG, Ri^{-1}) capture the role of thermal structure in sustaining CAT-favorable environments. Strong horizontal temperature gradients (HTG) maintain upper-level jet streams via thermal wind balance, while the inverse Richardson number (Ri^{-1}) serves as an effective proxy for the competition between shear production and buoyant suppression of turbulent kinetic energy. (3) Frontogenesis and deformation indices (e.g., Brown, Dutton, Ellrod) identify regions of active frontogenetical forcing and intense flow deformation near jet streaks. In these regions, the compression of thermal gradients can intensify local vertical shear and facilitate the downscale energy cascade from synoptic scales to turbulent eddy scales [35]. Collectively, these indices sample the primary physical pathways through which CAT is generated, ensuring broad diagnostic coverage of diverse meteorological environments.

The study area focused on Southwest China (20–45° N, 75–115° E), a region where multiple meteorological systems are superimposed, including upper-level jet streams, upper-level troughs, and gravity waves triggered by complex terrain (Figure 1). This environment makes it highly susceptible to aviation turbulence during flight. Turbulence is particularly severe along the routes from the Sichuan Basin to the Tibetan Plateau. To enhance the operational relevance of this study, a 2-degree-wide flight corridor covering the Chengdu–Lhasa route was established based on navigation data from the electronic Aeronautical Information Publication (eAIP). Based on topography, the corridor is divided into three segments: the Basin segment (>103.5° E), the Transition segment (100.0–103.5° E), and the Plateau segment (≤100.0° E). This segmentation enabled us to systematically analyze the changes in the response to CAT across different topographic steps.

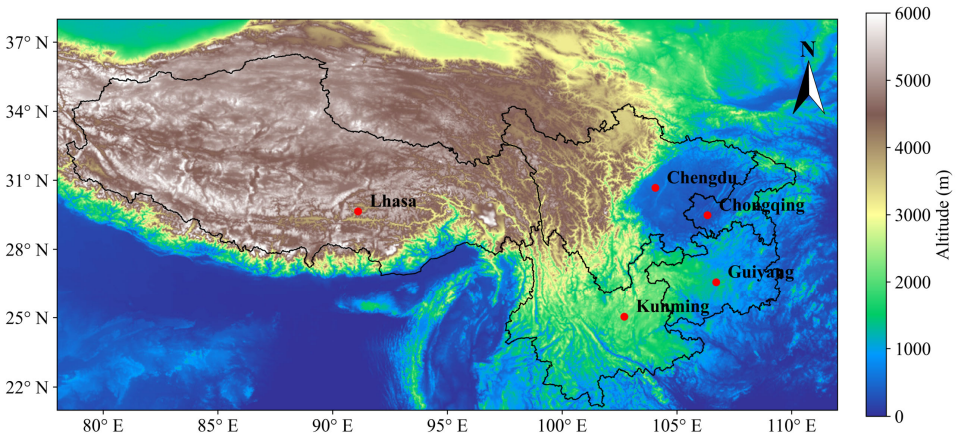

Figure 1. Topography of the study region in Southwest China. The map illustrates the Tibetan Plateau, the Sichuan Basin, and the Yunnan–Guizhou Plateau. Shading denotes surface elevation (m) as indicated by the color bar. Red markers show the locations of major cities, including Lhasa, Chengdu, Kunming, Chongqing, and Guiyang. Black solid lines indicate administrative boundaries.

Following the methodology of Williams [6], we constructed a baseline probability distribution by spatiotemporally pooling all daily samples of the diagnostic indices across all valid grid points within the study area during the historical period (1985–2014). These samples were derived directly from the NorESM2 historical simulations to establish six

turbulence intensity categories, yielding a total pool of over 37.7 million individual cases. The percentile intervals, corresponding occurrence frequencies, and the absolute number of historical cases for each category are detailed in Table 2, with intensity levels ranging from light (97.0th percentile) to severe (99.9th percentile). The calculated thresholds were subsequently applied to evaluate turbulence frequencies on both annual and seasonal (spring (March to May, MAM), summer (June to August, JJA), autumn (September to November, SON), and winter (December to February, DJF)) scales. To better quantify the turbulence frequency, MOG turbulence was introduced, which corresponds to the 99.6th percentile threshold in Table 2.

Table 2. Definition of turbulence intensity categories, corresponding percentile ranges, climatological occurrence frequencies, and the number of historical cases.

Turbulence Strength Category	Null	L	L-M	M	M-S	S
Percentile range (%)	0–97.0	97.0–99.1	99.1–99.6	99.6–99.8	99.8–99.9	99.9–100
Probability (%)	97.0	2.1	0.5	0.2	0.1	0.1
Number of Historical Cases	36,591,068	792,178	188,614	75,446	37,723	37,723

To evaluate future changes, we retained the historical thresholds which ensures that the projected frequency increases are directly comparable to past records. For the interannual analysis, we applied a 19-year running mean to all calculated time series, it helps to extract robust evolution signals and filter out interannual variability.

3. Results

3.1. Regional Characteristics and Historical Climatology of CAT

Figure 2 shows the historical climatological spatial distribution of MOG-CAT frequency at 250 hPa. The ensemble mean of the 15 independent diagnostics reveals a zonally oriented band of elevated MOG-CAT frequency near 30–35° N (Figure 2a), with annual frequencies reaching up to 1.6%. This belt is located close to the climatological axis of the East Asian Subtropical Westerly Jet (EASWJ). Local frequency maxima are found over the Hengduan Mountains at the junction of the Tibetan Plateau and the Yunnan–Guizhou Plateau, as well as over the Karakoram Mountains in the western Tibetan Plateau (Figure 2a). The spatial patterns of the individual diagnostics likewise exhibit a broad high-frequency band near 30–35° N, although differences remain in the magnitude and local structural details among the indices (Figure 2b–e). Specifically, the high-frequency regions diagnosed by Ellrod1 and the Dutton index are more spatially continuous, whereas the Ri^{-1} index displays a more pronounced gradient across the topographic transition zone (Figure 2d). The overall consistency among the different diagnostics provides a baseline reference for the subsequent scenario comparisons.

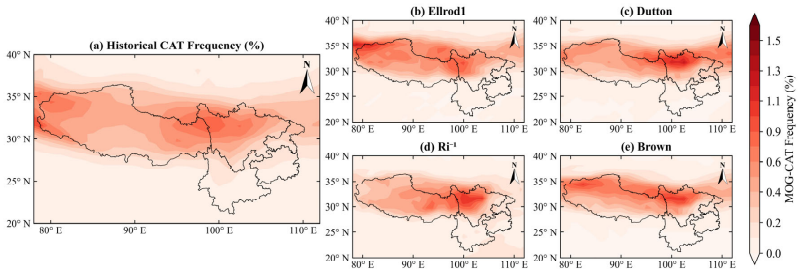

Figure 2. Spatial climatology of MOG-CAT frequency at 250 hPa during the historical period 1985–2014. (**a**) Multi-diagnostic ensemble mean across 15 independent CAT diagnostics; (**b**) Results from the Ellrod1 diagnostic; (**c**) Results from the Dutton diagnostic; (**d**) Results from the Ri-1 diagnostic; (**e**) Results from the Brown diagnostic. Shading denotes occurrence frequency (%).

Figure 3 presents the probability density functions (PDFs) of the 15 CAT diagnostics for the historical and future periods. During the historical period, the histograms of all CAT diagnostics generally exhibit positively skewed unimodal distributions. Under the high-emission scenarios, the probability distributions of most turbulence diagnostics shift rightward, implying an increased likelihood of encountering stronger turbulence. For most indices, the dominant future signal is an enhancement of the upper tail of the distribution. This feature is most pronounced in the late twenty-first century (2065–2094) under the SSP5-8.5 scenario. The relatively small differences in the low-to-median range indicate that the projected changes are characterized primarily by a tail-thickening effect rather than a systematic shift in the entire distribution. Diagnostics associated with wind shear and flow deformation, including VWS, DEF^2, Ellrod 1/2, the Brown index, and the Dutton index, as well as Ri^{-1}, exhibit particularly pronounced upper-tail amplification. These results suggest that the probability of extreme-intensity turbulence increases more substantially under the SSP5-8.5 scenario and toward the end of the twenty-first century.

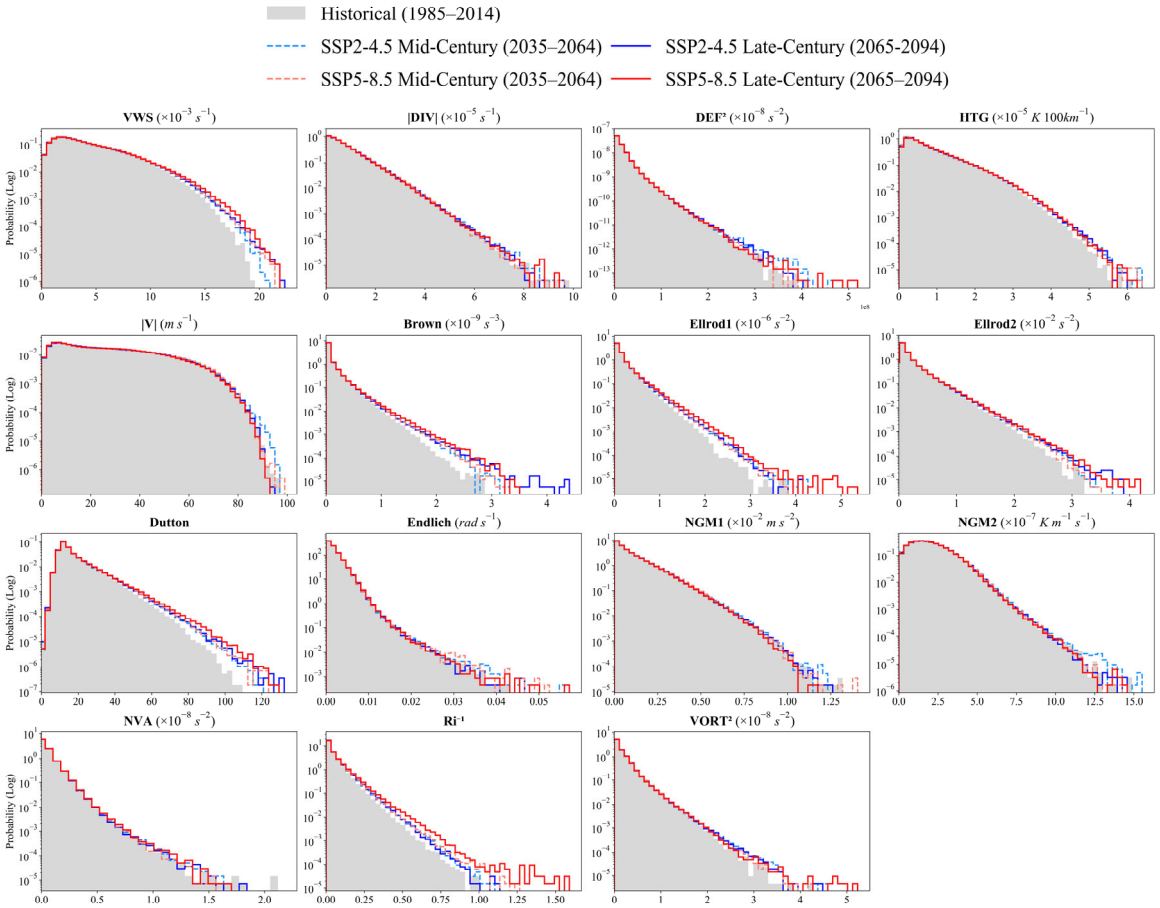

Figure 3. Probability density functions (PDFs) of the 15 CAT diagnostic indices at 250 hPa. Results are shown for the historical period 1985–2014 (gray) and for future projections under SSP2-4.5 (blue) and SSP58.5 (red). Dashed lines denote mid-century (2035–2064) projections; solid lines denote late-century (2065–2094) projections. The y-axis is plotted on a logarithmic scale.

To further assess the statistical robustness of the stretched upper tails shown in Figure 3, we quantified the relative increases in threshold exceedance probabilities together with their 95% confidence intervals (CIs) using bootstrap resampling. As shown in Figure 4, the uncertainty ranges remain generally well constrained. For several representative large-scale dynamical diagnostics, especially under the late-century SSP5-8.5 scenario, the lower bounds of the 95% CIs remain above zero. This suggests that the projected

increases in upper-tail exceedance probabilities are unlikely to be explained solely by sampling uncertainty.

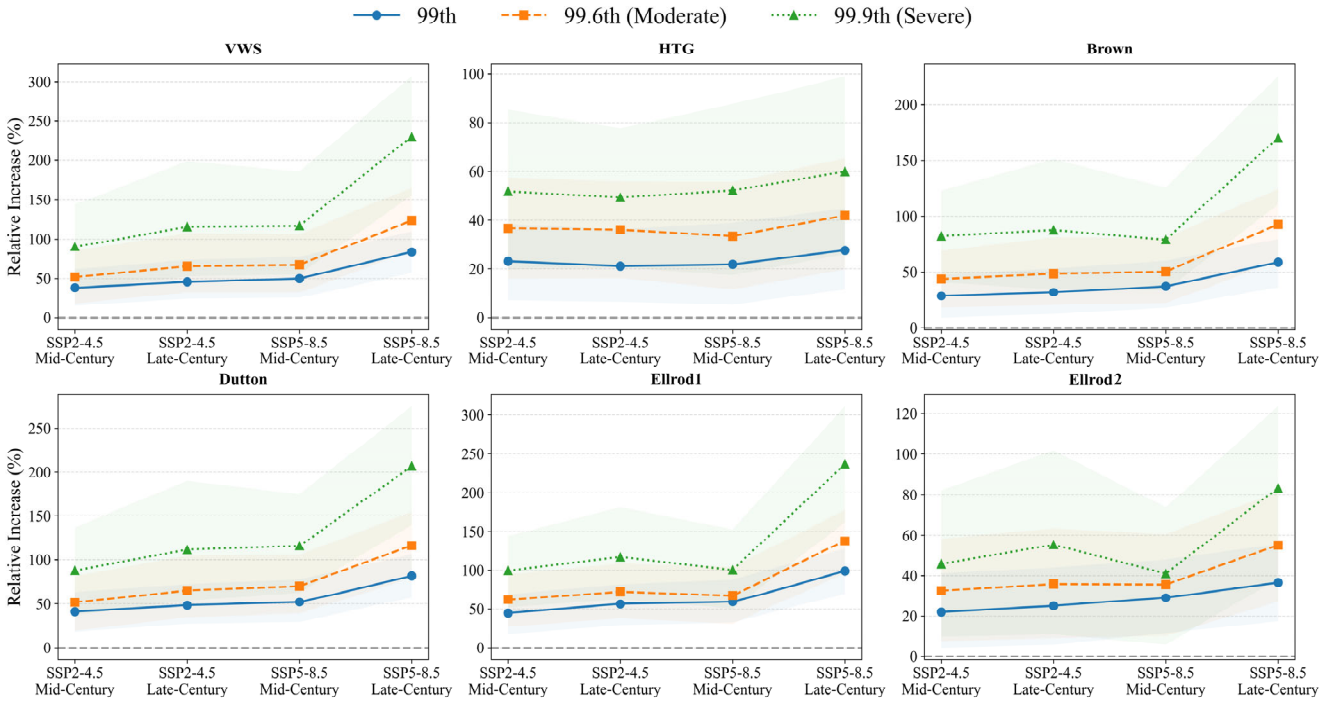

Figure 4. Projected relative increases in extreme clear-air turbulence (CAT) probabilities for six representative diagnostic indices across different future emission scenarios and periods. The blue, orange, and green lines represent the 99th, 99.6th (Moderate), and 99.9th (Severe) percentile thresholds, respectively, as defined by the 1985–2014 historical baseline. The corresponding shaded bands indicate the 95% confidence intervals derived from bootstrap resampling iterations. The zero-line represents the historical baseline with no relative change.

Figure 4 also shows that the relative increase in exceedance probability tends to be larger for rarer events. For example, for the VWS diagnostic under late-century SSP5-8.5, the exceedance probability above the 99th percentile increases by approximately 80%, whereas the exceedance probability above the 99.9th percentile increases by roughly 230%. Similar behavior is also found in several other representative diagnostics, including Brown, Dutton, and Ellrod1. Additional quantitative estimates for all selected diagnostics and thresholds are provided in Figure A1. Collectively, these results indicate that future changes are expressed more clearly in the upper tail of the CAT-favorable distributions, especially for the more extreme categories over Southwest China.

3.2. Spatiotemporal Evolution of Projected CAT Frequency

Figure 5 shows the spatial anomalies in MOG-CAT frequency relative to the 1985–2014 baseline period (ΔMOG-CAT frequency). Stippling denotes grid cells where at least 12 of the 15 diagnostics agree on the sign of change. Regions of pronounced MOG-CAT increase are concentrated near 30–35° N, coinciding with the historical high-frequency belt. Under the SSP2-4.5 scenario, the primary increase center in the mid-twenty-first century (2035–2064) is located over the Hengduan Mountains and the adjacent topographic transition zone (Figure 5a). By the late twenty-first century (2065–2094), this enhancement belt intensifies and extends zonally (Figure 5b). Larger increases are projected under the SSP5-8.5 scenario (Figure 5c,d), with local frequency increases reaching approximately 0.3–0.4% by the end of the century (Figure 5d).

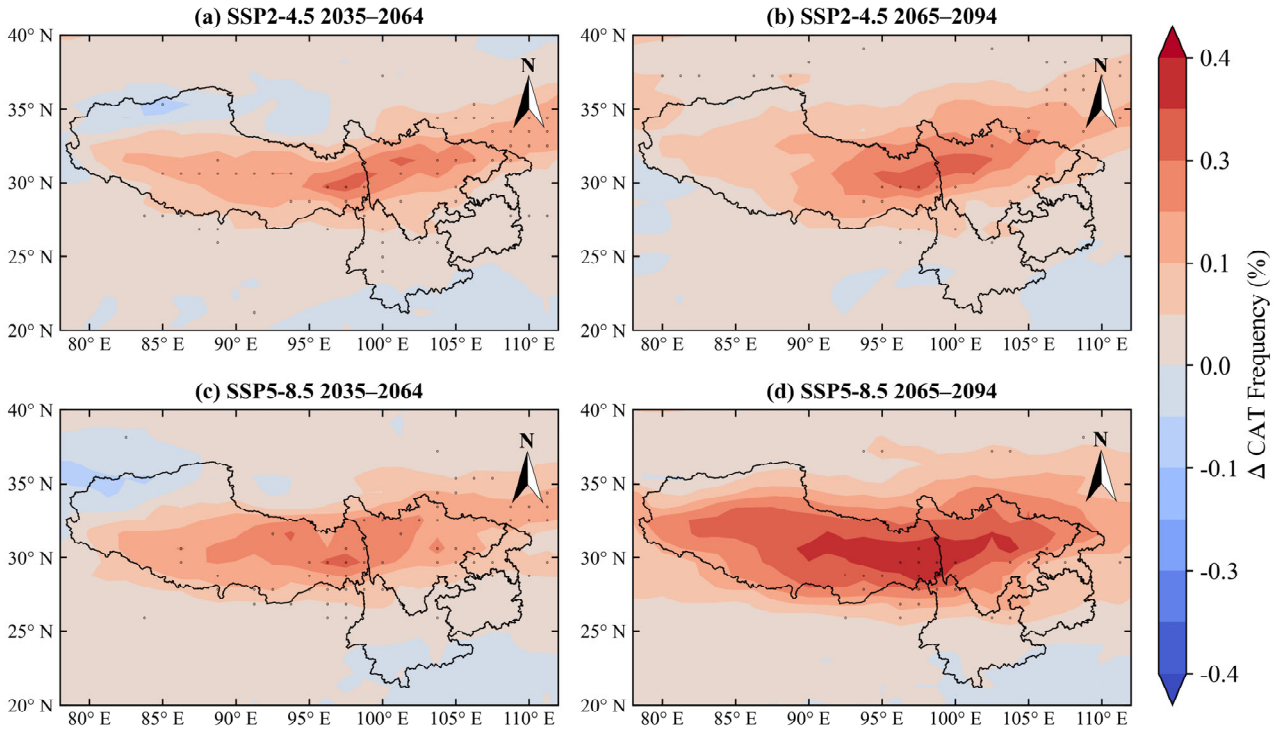

Figure 5. Projected anomalies in annual-mean MOG-CAT frequency at 250 hPa relative to the historical baseline 1985–2014. (**a**) Changes under SSP2-4.5 for mid-century (2035–2064); (**b**) Changes under SSP2-4.5 for late-century (2065–2094); (**c**) Changes under SSP5-8.5 for mid-century (2035–2064); (**d**) Changes under SSP5-8.5 for late-century (2065–2094). Shading denotes changes in frequency (%). Stippling marks grid cells where at least 12 of the 15 diagnostics agree on the sign of change.

3.3. Seasonal Variability and Shifts in CAT Intensity Categories

Figure 6 shows the seasonal anomalies in ΔMOG-CAT frequency for the late twenty-first century. From SON to MAM, both the spatial extent and magnitude of positive anomalies increase progressively, reaching a maximum in MAM, when the enhancement nearly spans the entire central latitudinal belt of the study region and locally reaches up to 6.5%. Areas marked by strong inter-diagnostic agreement are also primarily concentrated within these positive-anomaly regions. Compared with SSP2-4.5, SSP5-8.5 does not produce a substantial increase in anomaly magnitude, but it does lead to a further expansion of the area experiencing positive changes. In contrast, the JJA response exhibits pronounced spatial heterogeneity: positive anomalies are mainly confined to the Kunlun Mountains over the western Tibetan Plateau, whereas decreases occur over much of the Plateau interior and in parts of its eastern sector.

Figure 7a shows the 19-year moving-average time series of DJF MOG-CAT frequency. The historical period (1985–2014) exhibits a weak upward trend, while the trajectories under SSP2-4.5 and SSP5-8.5 begin to diverge around 2030. By the mid-twenty-first century (2035–2064), the frequency increase reaches 30.2% under SSP2-4.5 and 36.5% under SSP5-8.5. By the late twenty-first century (2065–2094), the increase under SSP2-4.5 decreases to 28.3%, whereas that under SSP5-8.5 more than doubles, rising to 69.4%. The turbulence-intensity category analysis (Figure 7b,c) further indicates that the magnitude of increase varies across intensity classes, with larger relative increases associated with stronger turbulence categories. Under SSP5-8.5, most diagnostics show a particularly pronounced increase in the frequency of severe events by the end of the century. Despite some inter-diagnostic spread, the majority of diagnostics consistently indicate increasing frequencies of MOG events.

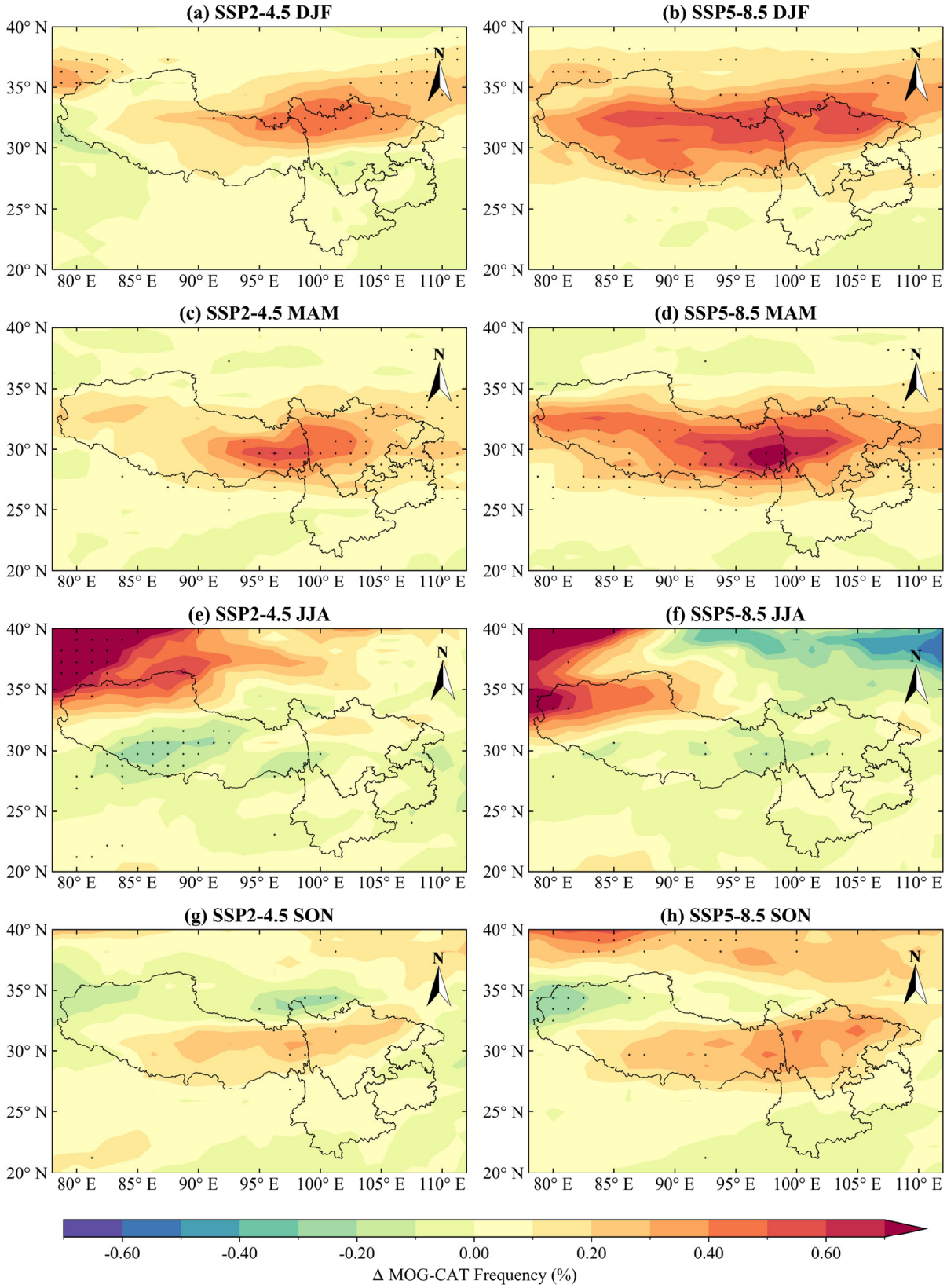

Figure 6. Projected seasonal-mean anomalies in MOG-CAT frequency at 250 hPa for the late-century (2065–2094) relative to the historical period (1985–2014). (**a**) DJF under SSP2-4.5; (**b**) DJF under SSP5-8.5; (**c**) MAM under SSP2-4.5; (**d**) MAM under SSP5-8.5; (**e**) JJA under SSP2-4.5; (**f**) JJA under SSP5-8.5; (**g**) SON under SSP2-4.5; (**h**) SON under SSP5-8.5. Shading denotes changes in frequency (%). Stippling marks grid cells where at least 12 of the 15 diagnostics agree on the sign of change.

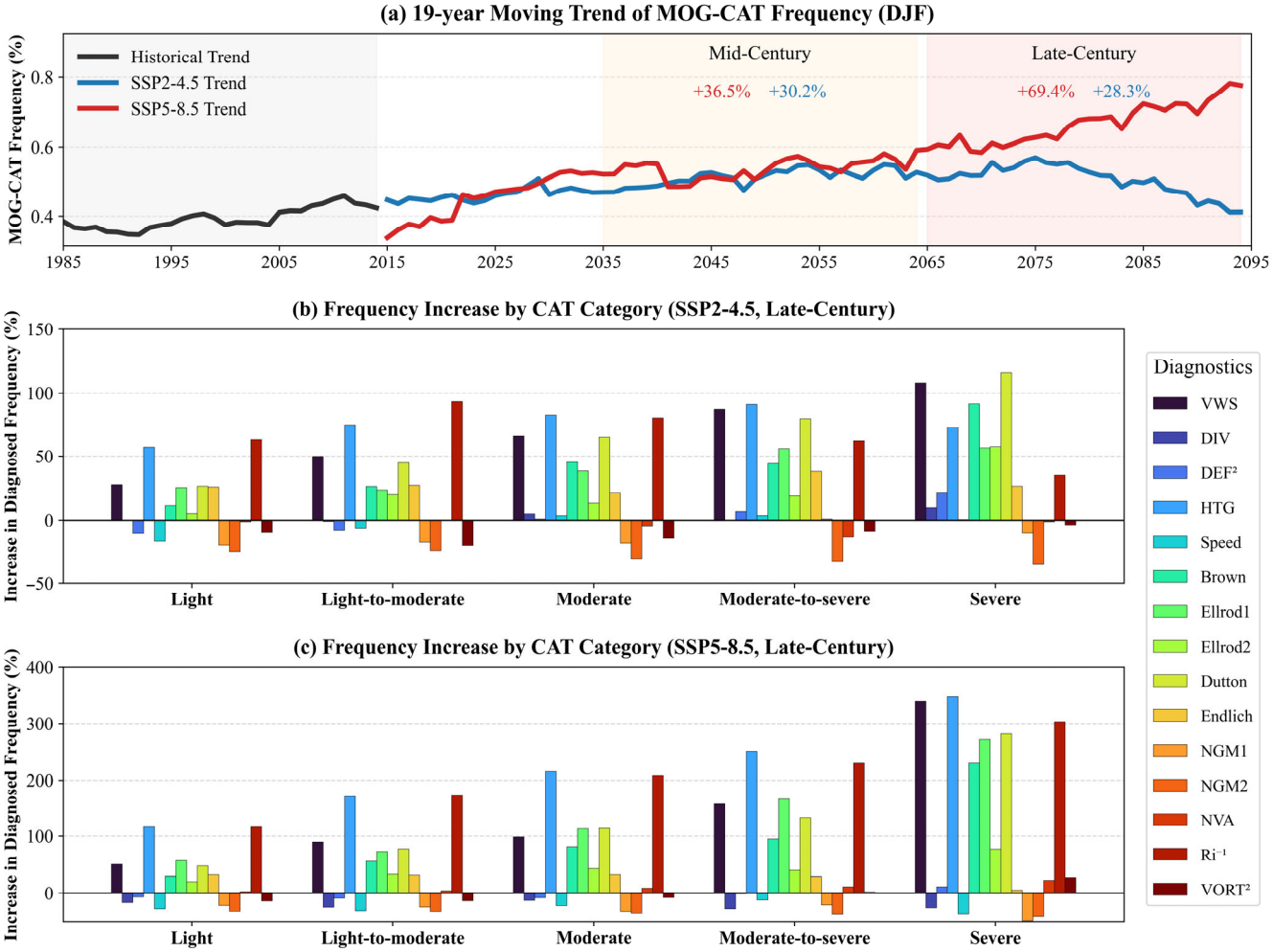

Figure 7. Temporal evolution and intensity-category changes in CAT frequency. (**a**) 19-year moving average of domain-mean DJF MOG-CAT frequency at 250 hPa from 1985 to 2094, with labeled relative changes for mid-century (2035–2064) and late-century (2065–2094) under SSP2-4.5 (blue) and SSP5-8.5 (red); (**b**) Relative changes in frequency (%) across CAT intensity categories from Light to Severe for late-century (2065–2094) under SSP2-4.5; (**c**) Relative changes in frequency (%) across CAT intensity categories from Light to Severe for late-century (2065–2094) under SSP5-8.5.

3.4. Route-Based Risk Assessment for the Chengdu–Lhasa Flight Corridor

We performed a corridor-based analysis to quantify the relative increase in DJF MOG-CAT frequency along the Chengdu Shuangliu–Lhasa Gonggar flight route. As shown in Figure 8b, the median change in MOG-CAT frequency is positive across all route segments and scenarios by the late twenty-first century. Under SSP2-4.5, the projected increases in all three segments are largely concentrated within 0–100%. In contrast, SSP5-8.5 exhibits larger median changes and a broader inter-diagnostic spread: the median increase is around 50% over both the Plateau and Basin segments, while the Transition segment shows the largest increase, reaching about 85%, with most diagnostics falling within the 50–180% range. Some diagnostics, particularly the HTG index, display notably large outliers in the Transition segment under SSP5-8.5. Nevertheless, more than 90% of the diagnostics indicate an increase in the same sign, suggesting a strong consensus regarding the future increase in turbulence frequency along the Chengdu–Lhasa corridor.

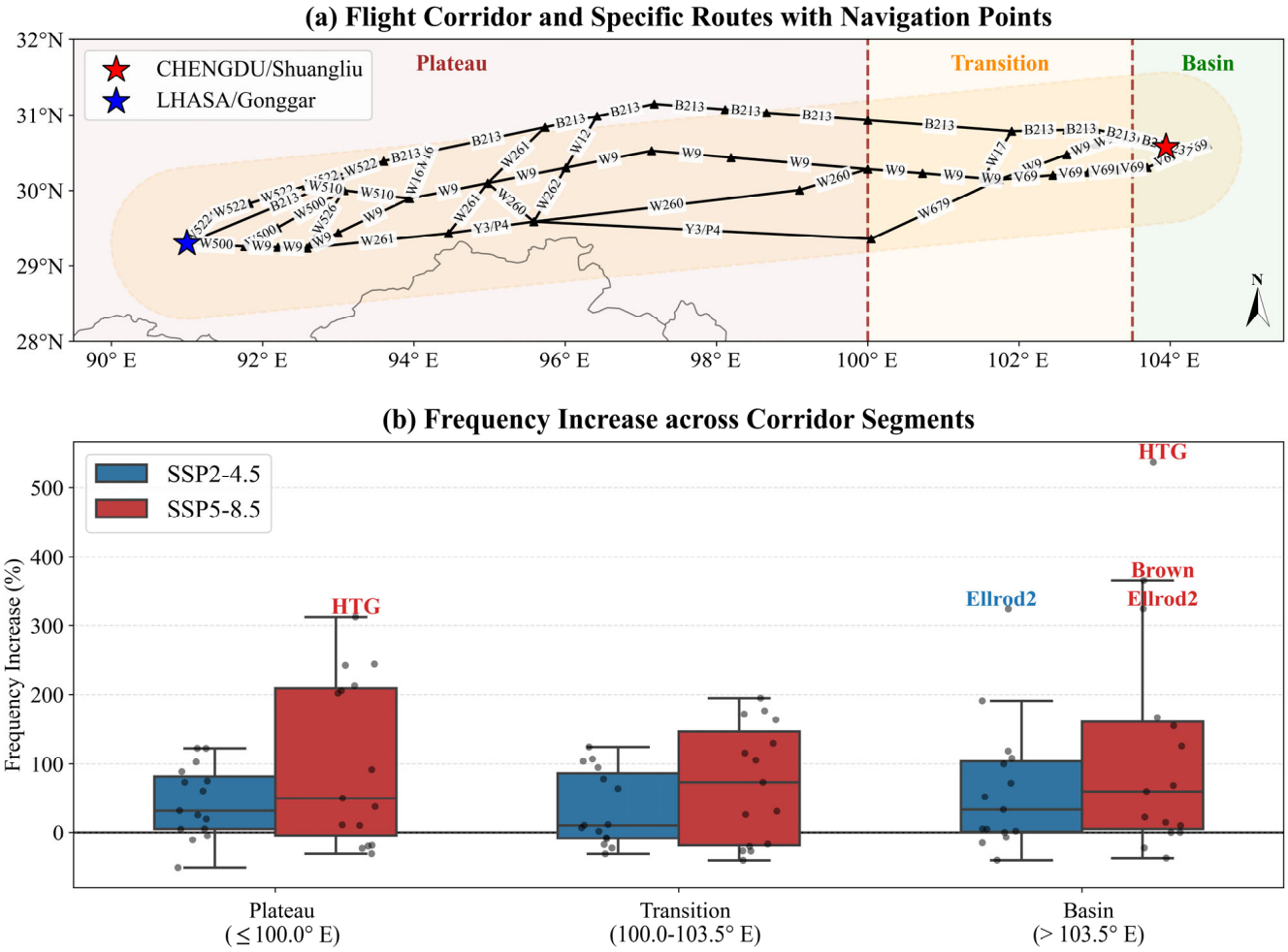

Figure 8. Route-based assessment along the Chengdu–Lhasa flight corridor. (**a**) The corridor derived from eAIP route and waypoint information and divided into three segments: Basin, Transition, and Plateau; (**b**) Relative changes (%) in DJF MOG-CAT frequency for the late-century (2065–2094) relative to the historical period (1985–2014) for each segment. Boxplots summarize the distribution across the 15 diagnostics, with dots representing individual diagnostics. Labeled points denote diagnostics lying beyond the whiskers (1.5 × IQR).

4. Discussion

NorESM2 projections indicate an overall increase in MOG-CAT frequency at 250 hPa over Southwest China during the 21st century, with larger increases under SSP5-8.5 than SSP2-4.5. This regional signal is broadly consistent with global-scale assessments reporting increasing upper-level turbulence in a warming climate [6,11,21]. Although the specific dynamical drivers were not explicitly evaluated here, the spatial patterns identify Southwest China as a region of pronounced projected increases in future turbulence frequency, particularly along the midlatitude band that overlaps the climatological corridor of the EASWJ.

The larger increases under SSP5-8.5, especially by the late century, are consistent with earlier studies relating turbulence changes to strengthened upper-level shear associated with large-scale thermal gradients. From a dynamical perspective, this trend is primarily driven by the strengthening and increased variability of the upper-level jet streams rather than their weakening. Recent research characterizes the response of the upper-level jet to climate change as a “fast-get-faster” mechanism. Driven by the nonlinear Clausius-Clapeyron relation and enhanced latitudinal density contrasts, upper-level westerly jet winds are projected to intensify while simultaneously exhibiting increased meridional

waviness [36]. Enhanced upper-tropospheric warming has also been shown to strengthen vertical wind shear at upper-level cruising altitudes [37]. A commonly cited interpretation invokes the Richardson number framework, in which changes in stability and shear can alter the likelihood of dynamically unstable conditions. However, diagnosing these terms explicitly is beyond the scope of the present analysis. In our results, the enhanced frequency changes near the topographic transition of the Tibetan Plateau are spatially collocated with the jet corridor, indicating that the strongest projected changes are concentrated there. In addition, the probability density functions show that historical–future differences are most evident in the upper tail, indicating that increases are concentrated under higher-intensity conditions. This upper-tail enhancement is consistent with prior findings that stronger turbulence categories tend to amplify more rapidly than the mean state [3,6,11].

From an operational perspective, seasonal contrast and route-based assessments reveal aviation-relevant heterogeneity. Along the Chengdu–Lhasa flight corridor, DJF MOG-CAT frequency increases across the Basin, Transition, and Plateau segments, with larger median increases and wider inter-diagnostic spread under SSP5-8.5. These changes suggest that turbulence-prone conditions may become more frequent along this high-impact route in winter, with potential implications for tactical avoidance and route-planning.

This study has several limitations. Although NorESM2 is among the higher-resolution models in CMIP6, it cannot explicitly resolve microscale turbulence or the full spectrum of terrain-related gravity-wave processes. The use of daily mean output may also smooth short-lived extremes relative to sub-daily data. Previous sensitivity analyses have nevertheless shown that daily mean output retains spatial and probability distributions similar to those of sub-daily output, supporting its use for climatological trend assessment [11]. The consistency across the 15 diagnostics, reflected in the ensemble-mean patterns and the agreement masks in the seasonal analysis, suggests that the main projected signals are robust despite structural model uncertainty. Future work using higher-frequency output, dynamical downscaling, and large-ensemble or multi-model analyses will help quantify internal variability and better constrain mesoscale contributions in this topographically complex region.

5. Conclusions

Based on projections from the NorESM2 model within the CMIP6 framework, the main conclusions are as follows:

(1) A zonally oriented belt of high MOG-CAT frequency is located near 30–35° N, with annual frequencies reaching up to 1.6%. Frequency maxima are mainly concentrated over the Hengduan Mountains at the junction of the Tibetan Plateau and the Yunnan–Guizhou Plateau, as well as over the Karakoram Mountains in the western Tibetan Plateau. Projections indicate that the principal future enhancement belt of MOG-CAT also remains concentrated in this region. Compared with SSP2-4.5, SSP5-8.5 exhibits both larger increases in magnitude and a broader spatial extent of the positive anomaly belt. The seasonal results further show that the largest increases occur in DJF and MAM, and the 15 diagnostics are generally consistent over the core enhancement regions. In contrast, during summer, most of the Plateau interior and parts of its eastern sector exhibit decreasing tendencies. Overall, these projected changes are spatially heterogeneous rather than spatially uniform, with the strongest increases concentrated along the pre-existing high-frequency belt.

(2) The projected changes are not uniform across turbulence intensity categories. Stronger turbulence categories exhibit larger relative increases in frequency. The probability density functions further show that the historical–future differences are most pronounced in the right tail of the distributions, indicating that the increase is concen-

trated primarily in more extreme turbulence conditions. The smoothed time series further indicate that, by the mid-twenty-first century, MOG-CAT increases by 30.2% under SSP2-4.5 and by 36.5% under SSP5-8.5. By the late twenty-first century, the increase under SSP2-4.5 decreases to 28.3%, whereas that under SSP5-8.5 nearly doubles to 69.4%.

(3) Along the Chengdu–Lhasa flight corridor, MOG-CAT frequency increases across the Basin, Transition, and Plateau segments under both scenarios. Under SSP5-8.5, the median increase across diagnostics is around 50% over both the Plateau and Basin segments, whereas the Transition segment shows the largest increase, reaching about 85%, with most diagnostics falling between 50% and 180%.

(4) In summary, this study finds that under future high-emission scenarios, there is a greater tendency for an increase in both the frequency and intensity of MOG-CAT across the southwestern region, exhibiting a pattern where higher emissions lead to more pronounced effects. Due to its topographic characteristics, the Transition segment demonstrates a stronger sensitivity to emission increases, resulting in a more intense anomalous response. Consequently, following an increase in emissions, flight routes in the southwestern region may encounter more frequent MOG-CAT, thereby increasing the difficulty of civil aviation warning and aviation safety assurance in this area.

Author Contributions: All authors contributed to the manuscript writing. R.Z. conceived the idea, designed the study, and wrote the original draft; Z.C., W.S., T.C. and Y.H. jointly supervised and guided this work; W.S. and Y.H. contributed to the manuscript review and editing. All authors have read and agreed to the published version of the manuscript.

Funding: This study was funded by the Key Open Laboratory on Aviation Meteorology of China Meteorological Administration, through the project "Research on Key Aviation Meteorological Support Technologies for Typical Low-altitude Scenarios" (No. HKQXZ-2025001), the project "Characteristic Analysis of Clear-air Turbulence in China and Its Projection Under Global Warming" (No. HKQXQ-2024002), and the Fundamental Research Funds for the Central Universities Grant PHD2023-023.

Institutional Review Board Statement: Not applicable.

Informed Consent Statement: Not applicable.

Data Availability Statement: All figures in this manuscript use the CMIP6 NorESM2-MM data available at https://esgf-node.llnl.gov/search/cmip6 (accessed on 20 August 2025). The DOIs of the NorESM2-MM datasets are https://doi.org/10.22033/ESGF/CMIP6.8040 (historical; accessed on 20 August 2025), http://doi.org/10.22033/ESGF/CMIP6.8255 (SSP2-4.5; accessed on 20 August 2025) and https://doi.org/10.22033/ESGF/CMIP6.8321 (SSP5-8.5; accessed on 20 August 2025).

Acknowledgments: During the preparation of this manuscript, the author used [Gemini, 3.1 pro] for the purposes of improve language. The authors have reviewed and edited the output and take full responsibility for the content of this publication.

Conflicts of Interest: The authors declare no conflicts of interest. The funders had no role in the design of the study; in the collection, analyses, or interpretation of data; in the writing of the manuscript; or in the decision to publish the results.

Abbreviations

The following abbreviations are used in this manuscript:

MOG	Moderate-or-Greater
CAT	Clear-air Turbulence
EASWJ	East Asian Subtropical Westerly Jet
eAIP	Aeronautical Information Publication

Spring	MAM
Summer	JJA
Autumn	SON
Winter	DJF

Appendix A

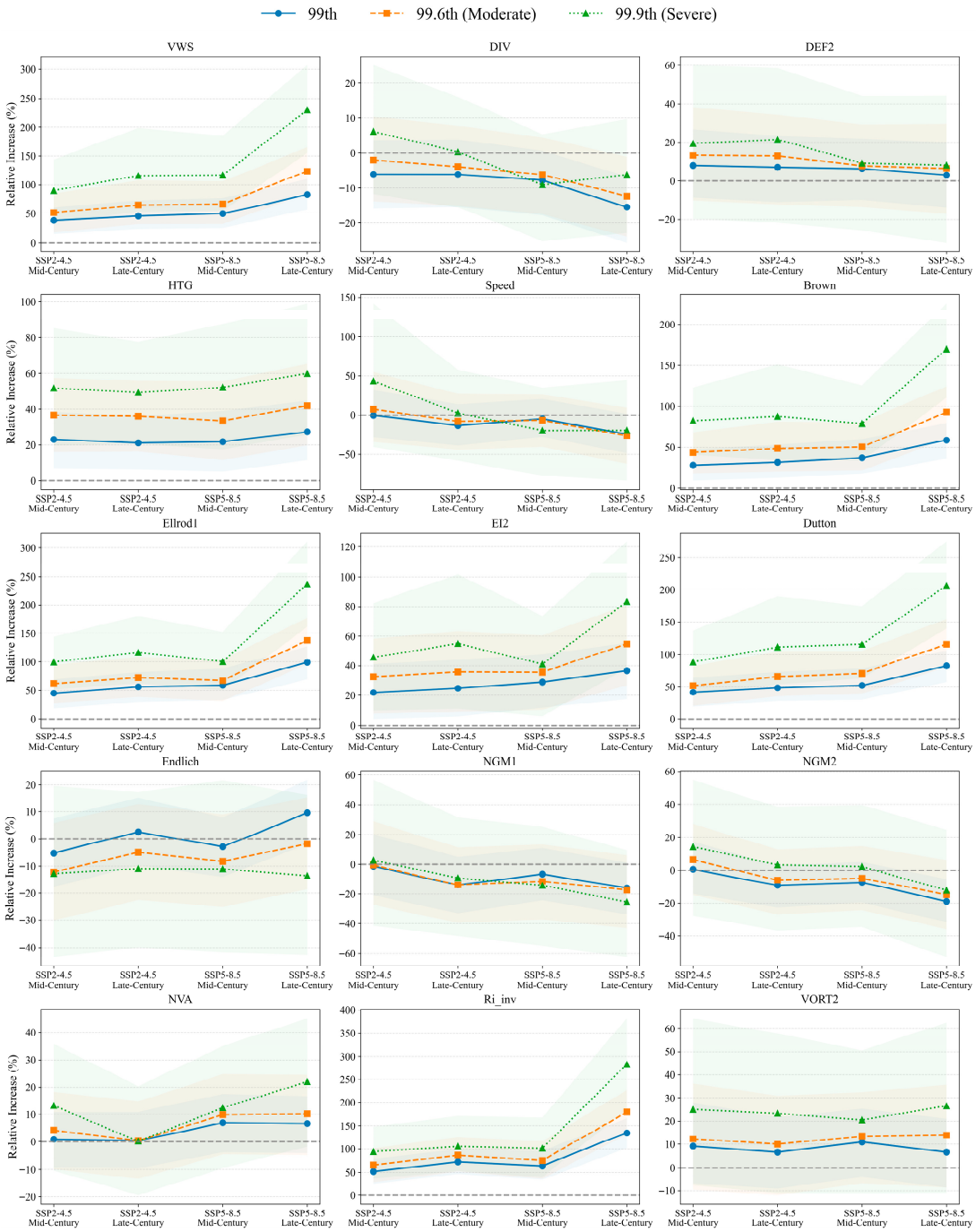

Figure A1. Projected relative increases in extreme clear-air turbulence (CAT) probabilities for all 15 diagnostic indices across different future emission scenarios and periods. The blue, orange, and green lines represent the 99th, 99.6th (Moderate), and 99.9th (Severe) percentile thresholds, respectively, as defined by the 1985–2014 historical baseline. The corresponding shaded bands indicate the 95% confidence intervals derived from bootstrap resampling iterations. The zero line represents the historical baseline with no relative change.

References

1. Chambers, E. Clear Air Turbulence and Civil Jet Operations. *J. R. Aeronaut. Soc.* **1955**, *59*, 613–628. [CrossRef]
2. Dutton, J.A.; Panofsky, H.A. Clear Air Turbulence: A Mystery May Be Unfolding. *Science* **1970**, *167*, 937–944. [CrossRef] [PubMed]
3. Williams, P.; Joshi, M. Intensification of winter transatlantic aviation turbulence in response to climate change. *Nat. Clim. Change* **2013**, *3*, 644–648. [CrossRef]
4. Atlas, D.; Metcalf, J.I.; Richter, J.H.; Gossard, E.E. The Birth of "CAT" and Microscale Turbulence. *J. Atmos. Sci.* **1970**, *27*, 903–913. [CrossRef]
5. Endlich, R.M. The Mesoscale Structure of Some Regions of Clear-Air Turbulence. *J. Appl. Meteorol.* **1964**, *3*, 261–276. [CrossRef]
6. Williams, P.D. Increased light, moderate, and severe clear-air turbulence in response to climate change. *Adv. Atmos. Sci.* **2017**, *34*, 576–586. [CrossRef]
7. Lee, S.H.; Williams, P.D.; Frame, T.H.A. Increased shear in the North Atlantic upper-level jet stream over the past four decades. *Nature* **2019**, *572*, 639–642. [CrossRef]
8. Yang, R.; Liu, H.; Li, K.; Yuan, S. A Numerical Study of Clear-Air Turbulence over North China on 6 June 2017. *Atmosphere* **2024**, *15*, 407. [CrossRef]
9. Hu, B.; Hui, P.; Ding, J.; Tang, J. Clear-Air Turbulence (CAT) Encounters on 13 November 2019 over Central and Eastern China: Numerical Simulation and Generation Mechanism. *Wea. Forecast.* **2023**, *38*, 1643–1660. [CrossRef]
10. Lv, Y.; Guo, J.; Li, J.; Han, Y.; Xu, H.; Guo, X.; Cao, L.; Gao, W. Increased turbulence in the Eurasian upper-level jet stream in winter: Past and future. *Earth Space Sci.* **2021**, *8*, e2020EA001556. [CrossRef]
11. Kim, S.-H.; Kim, J.-H.; Chun, H.-Y.; Sharman, R.D. Global response of upper-level aviation turbulence from various sources to climate change. *npj Clim. Atmos. Sci.* **2023**, *6*, 92. [CrossRef]
12. Zhang, F. Generation of Mesoscale Gravity Waves in Upper-Tropospheric Jet–Front Systems. *J. Atmos. Sci.* **2004**, *61*, 440–457. [CrossRef]
13. Kim, J.-H.; Chun, H.-Y.; Sharman, R.D.; Keller, T.L. Evaluations of Upper-Level Turbulence Diagnostics Performance Using the Graphical Turbulence Guidance (GTG) System and Pilot Reports (PIREPs) over East Asia. *J. Appl. Meteorol. Climatol.* **2011**, *50*, 1936–1951. [CrossRef]
14. Ford, R. Gravity wave radiation from vortex trains in rotating shallow water. *J. Fluid Mech.* **1994**, *281*, 81–118. [CrossRef]
15. Sharman, R.D.; Trier, S.B.; Lane, T.P.; Doyle, J.D. Sources and dynamics of turbulence in the upper troposphere and lower stratosphere: A review. *Geophys. Res. Lett.* **2012**, *39*, L12803. [CrossRef]
16. Reiter, E.R.; Nania, A. Jet-Stream Structure and Clear-Air Turbulence (CAT). *J. Appl. Meteorol.* **1964**, *3*, 247–260. [CrossRef]
17. Woiwode, W.; Dörnbrack, A.; Geldenhuys, M.; Friedl-Vallon, F.; Giez, A.; Gulde, T.; Höpfner, M.; Johansson, S.; Kaifler, B.; Kleinert, A.; et al. Non-orographic gravity waves and turbulence caused by merging jet streams. *J. Geophys. Res. Atmos.* **2023**, *128*, e2022JD038097. [CrossRef]
18. Kao, S.-K.; Sizoo, A.H. Analysis of clear air turbulence near the jet stream. *J. Geophys. Res.* **1966**, *71*, 3799–3805. [CrossRef]
19. Foudad, M.; Sanchez-Gomez, E.; Jaravel, T.; Rochoux, M.C.; Terray, L. Past and future trends in clear-air turbulence over the northern hemisphere. *J. Geophys. Res. Atmos.* **2024**, *129*, e2023JD040261. [CrossRef]
20. Ito, S.; Miyamoto, Y.; Kajikawa, Y. Environmental fields of moderate clear air turbulence above 400 hPa around Japan. *Atmos. Sci. Lett.* **2025**, *26*, e1292. [CrossRef]
21. Storer, L.N.; Williams, P.D.; Joshi, M.M. Global response of clear-air turbulence to climate change. *Geophys. Res. Lett.* **2017**, *44*, 9976–9984. [CrossRef]
22. Smith, I.H.; Williams, P.D.; Schiemann, R. Clear-air turbulence trends over the North Atlantic in high-resolution climate models. *Clim. Dyn.* **2023**, *61*, 3063–3079. [CrossRef]
23. Prosser, M.C.; Williams, P.D.; Marlton, G.J.; Harrison, R.G. Evidence for large increases in clear-air turbulence over the past four decades. *Geophys. Res. Lett.* **2023**, *50*, e2023GL103814. [CrossRef]
24. Jaeger, E.B.; Sprenger, M. A Northern Hemispheric climatology of indices for clear air turbulence in the tropopause region derived from ERA40 reanalysis data. *J. Geophys. Res.* **2007**, *112*, D20106. [CrossRef]
25. Williams, P.D.; Storer, L.N. Can a climate model successfully diagnose clear-air turbulence and its response to climate change? *Q. J. R. Meteorol. Soc.* **2022**, *148*, 1424–1438. [CrossRef]
26. Hu, B.; Tang, J.; Ding, J.; Liu, G. Regional downscaled future change of clear-air turbulence over East Asia under RCP8.5 scenario within the CORDEX-EA-II project. *Int. J. Climatol.* **2021**, *41*, 5022–5035. [CrossRef]
27. Bock, L.; Lauer, A.; Schlund, M.; Barreiro, M.; Bellouin, N.; Jones, C.; Meehl, G.A.; Predoi, V.; Roberts, M.J.; Eyring, V. Quantifying progress across different CMIP phases with the ESMValTool. *J. Geophys. Res. Atmos.* **2020**, *125*, e2019JD032321. [CrossRef]
28. Bentsen, M.; Oliviè, D.J.L.; Seland, Ø.; Toniazzo, T.; Gjermundsen, A.; Graff, L.S.; Debernard, J.B.; Gupta, A.K.; He, Y.; Kirkevåg, A.; et al. NCC NorESM2-MM model output prepared for CMIP6 CMIP historical. *Earth Syst. Grid Fed.* **2019**. [CrossRef]
29. Bentsen, M.; Oliviè, D.J.L.; Seland, Ø.; Toniazzo, T.; Gjermundsen, A.; Graff, L.S.; Debernard, J.B.; Gupta, A.K.; He, Y.; Kirkevåg, A.; et al. NCC NorESM2-MM model output prepared for CMIP6 ScenarioMIP ssp245. *Earth Syst. Grid Fed.* **2019**. [CrossRef]

30. Bentsen, M.; Oliviè, D.J.L.; Seland, Ø.; Toniazzo, T.; Gjermundsen, A.; Graff, L.S.; Debernard, J.B.; Gupta, A.K.; He, Y.; Kirkevåg, A.; et al. NCC NorESM2-MM model output prepared for CMIP6 ScenarioMIP ssp585. *Earth Syst. Grid Fed.* **2019**. [CrossRef]
31. Gleckler, P.J.; Taylor, K.E.; Doutriaux, C. Performance metrics for climate models. *J. Geophys. Res.* **2008**, *113*, D06104. [CrossRef]
32. Taylor, K.E. Summarizing multiple aspects of model performance in a single diagram. *J. Geophys. Res.* **2001**, *106*, 7183–7192. [CrossRef]
33. Sharman, R.; Tebaldi, C.; Wiener, G.; Wolff, J. An Integrated Approach to Mid- and Upper-Level Turbulence Forecasting. *Wea. Forecast.* **2006**, *21*, 268–287. [CrossRef]
34. Sharman, R.D.; Pearson, J.M. Prediction of Energy Dissipation Rates for Aviation Turbulence. Part I: Forecasting Nonconvective Turbulence. *J. Appl. Meteorol. Climatol.* **2017**, *56*, 317–337. [CrossRef]
35. Ellrod, G.P.; Knapp, D.I. An Objective Clear-Air Turbulence Forecasting Technique: Verification and Operational Use. *Wea. Forecast.* **1992**, *7*, 150–165. [CrossRef]
36. Shaw, T.A.; Miyawaki, O.; Chou, H.-H.; Blackport, R. Fast-get-faster explains wavier upper-level jet stream under climate change. *Commun. Earth Environ.* **2024**, *5*, 653. [CrossRef]
37. de Medeiros, J.; Williams, P.D. Future Trends in Upper-Atmospheric Shear Instability from Climate Change. *J. Atmos. Sci.* **2025**, *82*, 2375–2392. [CrossRef]

Disclaimer/Publisher's Note: The statements, opinions and data contained in all publications are solely those of the individual author(s) and contributor(s) and not of MDPI and/or the editor(s). MDPI and/or the editor(s) disclaim responsibility for any injury to people or property resulting from any ideas, methods, instructions or products referred to in the content.